PERGAMON

International Journal of Solids and Structures 38 (2001) 5509–5526

INTERNATIONAL JOURNAL OF SOLIDS and STRUCTURES

www.elsevier.com/locate/ijsolstr

Application of material forces to hyperelastostatic fracture mechanics. II. Computational setting

P. Steinmann *, D. Ackermann, F.J. Barth

Lehrstuhl für Technische Mechanik, Universität Kaiserslautern, P.O. Box 3049, D-67653 Kaiserslautern, Germany

Received 6 July 2000; in revised form 29 September 2000

Dedicated to the occasion of the 60th birthday of Professor Dr.-Ing. D. Gross

Abstract

The concern of this work is a novel algorithmic treatment of hyperelastostatic fracture mechanics problems consistent to the notion of material forces within the geometrically nonlinear setting of continuum mechanics. To this end, we consider the continuum mechanics of material forces, as outlined in Part I of this work (P. Steinmann, Int. J. Solid Struct. 37, 7371–7391), which act, contrary to the common physical forces, on the material manifold or rather in the material space. In the sequel it is proposed to discretize the corresponding quasi-static balance of pseudo momentum by a standard Galerkin finite element procedure. As a result we obtain global discrete node point quantities, the material node point forces, which prove to be of the same qualitative and quantitative importance for the assessment of fracture mechanics problems as the classical J-integral.

Keywords: Material forces; Fracture mechanics; Computational setting

1. Introduction

A number of computational strategies to compute quantities relevant to the assessment of fractured configurations of hyperelastic materials have been proposed in the past. Relevant strategies based on the finite element method may essentially be classified in the following categories:

Energy release rate methods: Based on the conceptual relation between the energy release rate and stress intensity factors Parks (1974, 1977) and Hellen (1975) proposed to compute crack tip stress intensity factors from the energy release rates associated with virtual crack extensions based on derivatives of linear elastic finite element stiffness matrices. Later de Lorenzi (1982, 1985) improved the method of virtual crack extension by considering the energy release rates directly within a continuum. The aforementioned methods differ in detail, nevertheless their common conceptual basis is the consideration of the energy changes within a continuum upon (virtual) extension of the crack length.

* Corresponding author. Tel.: +49-631-205-2421; fax: +49-631-205-2128.
E-mail address: ps@rhrk.uni-kl.de (P. Steinmann).

0020-7683/01/$ - see front matter
PII: S0020-7683(00)00381-4

Contour integral methods: By the way of contrast, the numerical strategy applied e.g. by Shih and Needleman (1984a,b) relies on the direct evaluation of the path-independent J-integral, commonly credited to Rice (1968), by integrating the relevant quantities of the field solution obtained by solving the discretized direct motion problem along prescribed integration contours. Clearly this procedure demands additional data structures within a finite element post processor. Thereby two different options are available: either the integration contour follows the element edges or the integration contour directly connects the quadrature points of adjacent elements. In the first case additional projections from the quadrature points to the node points, e.g. by smoothing based on a least square fit, are necessary.

Domain integral methods: The close relation between the familiar contour and a specific domain representation of the J-integral has been exploited by Li et al. (1985) and Shih et al. (1986) to propose the so called energy domain integral as a particular virtual crack extension method. Thereby, after the selection of virtual node point quantities, which is reported to be uncritical, the solution obtained from the direct motion problem can be used directly without the need for additional data structures to compute the value of J. This very successful approach is implemented today as well in a number of commercial finite element packages. The theoretical background for the energy domain integral was developed for more general conditions by Moran and Shih (1987).

For any of the aforementioned strategies an appropriate mesh design is reported to be crucial for accurate results pertaining to the assessment of the fracture mechanics problem, see e.g. Shih et al. (1986) or Anderson (1995). Thereby, finite element designs which mimic the characteristic singularities of the stress/strain fields in the vicinity of the crack tip turned out to render sufficiently accurate predictions. Recall as the paradigm the quadratic $S2$-serendipity element with edge nodes moved to the quarter points which captures the $r^{-(1/2)}$ singularity typical for linear elastic scenarios. Nevertheless, in the nonlinear regime the degree of the singularities is most often not known in advance and no particular recommendation apart from using sufficiently refined meshes around the crack tip can be given under these general conditions.

It is the objective of this work to propose a novel computational strategy for the assessment of hyperelastostatic fractured configurations which is equally applicable within the geometrically linear and nonlinear setting. Thereby, we base our developments on the consequent exploitation of the concept of material forces. Contrary to physical forces, material forces represent the tendency of defects like e.g. cracks or inclusions to move relative to the ambient material. The necessary theoretical basis for the present endeavour together with the notation and terminology are taken from Part I of this work (Steinmann, 2001). An comprehensive treatment which promotes the concept of material forces based on the consideration of material inhomogeneities in elasticity is presented in the milestone monograph by Maugin (1993), see also the references therein. Based on our advocated approach we essentially aim in a quantitative comparison with classical J-integral evaluations and in an investigation of the influence of the discretization on the accuracy. Moreover we want to emphasize that the new method has the advantages that it requires no additional FE data structure, is extremely versatile, renders additional indicators for the geometrical shape sensitivity of the specimen and renders additional indicators for the mesh quality.

To this end, the paper is organized as follows: In Section 2 the relevant kinematic quantities and balance laws pertaining to the common physical and its complementary material viewpoint are briefly reiterated. Next, Section 3 develops the corresponding weak forms of the balance equations as the prerequisite for the finite element discretization elaborated upon in Section 4. Here the discrete so-called material node point forces are proposed for the assessment of fractured configurations of hyperelastic material. Then, based on the introduced notation and terminology, Section 5 compares different methods in computational fracture mechanics. Finally, Section 6 highlights the performance of the advocated material node point force method for a number of geometrically linear and nonlinear examples. The conclusions in Section 7 close the paper.

2. Strong form of quasi-static balance equations

A detailed treatment of the formulation of the physical and material balance laws has been given for the hyperelastostatic case in Part I of this work (Steinmann, 2001). Therefore we shall merely summarize the relevant statements needed in the sequel.

In the direct motion description the placement $\boldsymbol{x}$ of a material particle in the current configuration $\mathscr{B}$ is described by the nonlinear direct deformation map $\boldsymbol{x}=\boldsymbol{\varphi}(\boldsymbol{X})$ in terms of the placement $\boldsymbol{X}$ of the same material particle in the reference configuration $\mathscr{B}_0$. Vice versa, in the inverse motion description the placement $\boldsymbol{X}$ of a material particle in the reference configuration $\mathscr{B}_0$ is described by the nonlinear inverse deformation map $\boldsymbol{X}=\boldsymbol{\phi}(\boldsymbol{x})$ in terms of the placement $\boldsymbol{x}$ of the same material particle in the current configuration $\mathscr{B}$. The direct and inverse deformation gradients, i.e. the linear tangent maps associated to the direct and inverse deformations, together with their determinants are denoted by $\boldsymbol{F}=\nabla_X\boldsymbol{\varphi}$ and $\boldsymbol{f}=\nabla_x\boldsymbol{\phi}$ with $J=\det\boldsymbol{F}$ and $j=\det\boldsymbol{f}$, respectively.

The physical and material quasi-static balance equations of linear and pseudo momentum pertaining to the direct motion and inverse motion point of view, respectively, then follow as

$$-\mathrm{div}\boldsymbol{\sigma}^{\mathrm{t}}=\boldsymbol{b}^{\mathrm{phy}}\quad\text{and}\quad-\mathrm{Div}\boldsymbol{M}^{\mathrm{t}}=\boldsymbol{B}^{\mathrm{mat}}\tag{1}$$

Here $\boldsymbol{\sigma}$ and $\boldsymbol{M}$ denote the spatial Cauchy and the material Eshelby stress which may be derived for the hyperelastic case from the stored energy density $\mathscr{W}_0$ or $\mathscr{W}$

$$\boldsymbol{\sigma}^{\mathrm{t}}=j\partial_{\boldsymbol{F}}\mathscr{W}_0\cdot\boldsymbol{F}^{\mathrm{t}}=\mathscr{W}\boldsymbol{I}-\boldsymbol{f}^{\mathrm{t}}\cdot\partial_{\boldsymbol{f}}\mathscr{W}\quad\text{and}\quad\boldsymbol{M}^{\mathrm{t}}=J\partial_{\boldsymbol{f}}\mathscr{W}\cdot\boldsymbol{f}^{\mathrm{t}}=\mathscr{W}_0\boldsymbol{I}-\boldsymbol{F}^{\mathrm{t}}\cdot\partial_{\boldsymbol{F}}\mathscr{W}_0\tag{2}$$

Obviously, the stored energy is defined either per unit volume in $\mathscr{B}_0$ or per unit volume in $\mathscr{B}$, i.e. $\mathscr{W}_0=\mathscr{W}_0(\boldsymbol{F};\boldsymbol{X})$ or $\mathscr{W}=\mathscr{W}(\boldsymbol{f};\boldsymbol{X})$, respectively. Recall that the symmetry of $\boldsymbol{\sigma}$ is always mandatory due to requirement of physical objectivity whereas the symmetry of $\boldsymbol{M}$ is optional only in the case of material objectivity, i.e. for isotropic material. Finally, the right-hand sides of Eq. (1) are related by $\boldsymbol{B}^{\mathrm{mat}}=-\partial_{\boldsymbol{X}}\mathscr{W}_0-J\boldsymbol{F}^{\mathrm{t}}\cdot\boldsymbol{b}^{\mathrm{phy}}$. Thereby $\boldsymbol{b}^{\mathrm{phy}}$ are the physical volume forces, e.g. gravity, and $\partial_{\boldsymbol{X}}\mathscr{W}_0$ denotes the explicit material gradient of the stored energy density which is e.g. due to an inhomogeneous distribution of material constants over $\mathscr{B}_0$.

Remark 2.1. It shall be noted carefully that the vectorial residua of the quasi-static balances of physical and pseudo momentum have components in either physical or material space, respectively. Moreover, please recall that the quasi-static balances of physical and pseudo momentum serve for solving either the direct motion problem or the inverse motion problem, respectively. Thereby, the inverse motion problem is considered in a post processing computation since the material forces are only known a posteriori, i.e. when the direct motion problem has already been solved.

3. Weak form of quasi-static balance equations

As a prerequisite for a finite element discretization advocated in the sequel we consider the quasi-static balances of physical and pseudo momentum in their weak or rather variational form. The test functions $\boldsymbol{w}$ and $\boldsymbol{W}$ take the interpretations as the physical and material virtual displacements, respectively, and are assumed to satisfy the necessary smoothness and boundary requirements.

$$S^{\mathrm{sur}}=S^{\mathrm{int}}-S^{\mathrm{vol}}\quad\forall\boldsymbol{w}\tag{3a}$$

$$M^{\mathrm{sur}}=M^{\mathrm{int}}-M^{\mathrm{vol}}\quad\forall\boldsymbol{W}\tag{3b}$$

Thereby the surface contributions denote the physical and material variation, respectively, of the total bulk potential energy due to its complete dependence on the position in physical and material space, respectively, and are defined as

$$S^{\text{sur}} = \int_{\partial\mathscr{B}} \boldsymbol{w} \cdot \boldsymbol{\sigma}^{\text{t}} \cdot \boldsymbol{n}\,\mathrm{d}a \quad \text{and} \quad M^{\text{sur}} = \int_{\partial\mathscr{B}_0} \boldsymbol{W} \cdot \boldsymbol{M}^{\text{t}} \cdot \boldsymbol{N}\,\mathrm{d}A \tag{4}$$

For an account on the notion of physical and material variations please refer to Part I of this work (Steinmann, 2001). Furthermore, the internal contributions denote the physical and material variation, respectively, of the total bulk potential energy due to its implicit dependence on the position in physical and material space, respectively, and are defined as

$$S^{\text{int}} = \int_{\mathscr{B}} \nabla_x \boldsymbol{w} : \boldsymbol{\sigma}^{\text{t}}\,\mathrm{d}v \tag{5a}$$

$$M^{\text{int}} = \int_{\mathscr{B}_0} \nabla_X \boldsymbol{W} : \boldsymbol{M}^{\text{t}}\,\mathrm{d}V \tag{5b}$$

Likewise, the volume contributions denote the physical and material variation, respectively, of the total bulk potential energy due to its explicit dependence on the position in physical and material space, respectively, and are defined as

$$S^{\text{vol}} = \int_{\mathscr{B}} \boldsymbol{w} \cdot \boldsymbol{b}^{\text{phy}}\,\mathrm{d}v \quad \text{and} \quad M^{\text{vol}} = \int_{\mathscr{B}_0} \boldsymbol{W} \cdot \boldsymbol{B}^{\text{mat}}\,\mathrm{d}V \tag{6}$$

The particular energetic interpretations alluded to above for the different terms involved in the weak form have been discussed in detail in Part I of this work (Steinmann, 2001).

Remark 3.1. A fundamental difference between the direct and the inverse motion description are the Neumann boundary conditions. For the direct motion problem the physical boundary tractions are given input data whereas for the inverse motion problem the material boundary tractions can only be computed after the direct motion problem has been solved. Nevertheless this poses no difficulties since we consider the inverse motion problem only in a post processing computation.

4. Discretized form of quasi-static balance equations

The variational formats of the quasi-static balances of physical and pseudo momentum in Eqs. (3a) and (3b) lend themselves readily for a straightforward Galerkin discretization.

To this end we discretize the domain in n_{el} elements with $\mathscr{B}^h = \cup_{e=1}^{n_{\text{el}}} \mathscr{B}_e$ and $\mathscr{B}_0^h = \cup_{e=1}^{n_{\text{el}}} \mathscr{B}_{0e}$. On each element the geometry in $\mathscr{B}$ and $\mathscr{B}_0$ is interpolated from the positions $\boldsymbol{x}_n$ and $\boldsymbol{X}_n$ of the n_{en} nodes by shape functions N^n, with $n \in [1, n_{en}]$ denoting the local node numbering, as

$$\boldsymbol{x}^h \mid_{\mathscr{B}_e} = \sum_{n=1}^{n_{en}} N^n \boldsymbol{x}_n \quad \text{and} \quad \boldsymbol{X}^h \mid_{\mathscr{B}_{0e}} = \sum_{n=1}^{n_{en}} N^n \boldsymbol{X}_n \tag{7}$$

The shape functions obey the completeness condition $\sum_{n=1}^{n_{en}} N^n = 1$, the assembly of the elementwise expansions renders a globally C^0-continuous interpolation. Consequently, the deformation gradients on each element follow immediately as

$$\nabla_X \boldsymbol{x}^h \,|_{\mathscr{B}_e} = \sum_{n=1}^{n_{en}} \boldsymbol{x}_n \otimes \nabla_X N^n \quad \text{and} \quad \nabla_x \boldsymbol{X}^h \,|_{\mathscr{B}_{0e}} = \sum_{n=1}^{n_{en}} \boldsymbol{X}_n \otimes \nabla_x N^n$$

Next the elementwise discretization of the virtual physical and material displacement fields $\boldsymbol{w}$ and $\boldsymbol{W}$ into nodal values $\boldsymbol{w}_n$ and $\boldsymbol{W}_n$, which are interpolated by the same shape functions N^n in the spirit of an isoparametric expansion, renders the representations

$$\boldsymbol{w}^h \,|_{\mathscr{B}_e} = \sum_{n=1}^{n_{en}} N^n \boldsymbol{w}_n \quad \text{and} \quad \boldsymbol{W}^h \,|_{\mathscr{B}_{0e}} = \sum_{n=1}^{n_{en}} N^n \boldsymbol{W}_n \tag{8}$$

The corresponding gradients appearing in Eqs. (5a) and (5b) are thus given by

$$\nabla_x \boldsymbol{w}^h \,|_{\mathscr{B}_e} = \sum_{n=1}^{n_{en}} \boldsymbol{w}_n \otimes \nabla_x N^n \quad \text{and} \quad \nabla_X \boldsymbol{W}^h \,|_{\mathscr{B}_{0e}} = \sum_{n=1}^{n_{en}} \boldsymbol{W}_n \otimes \nabla_X N^n$$

Then the discretized contributions to the physical and material virtual work follow as

$$S^{\text{int}} = \sum_{e=1}^{n_{\text{el}}} S_e^{\text{int}}, \qquad S^{\text{vol}} = \sum_{e=1}^{n_{\text{el}}} S_e^{\text{vol}} \quad \text{and} \quad M^{\text{int}} = \sum_{e=1}^{n_{\text{el}}} M_e^{\text{int}}, \qquad M^{\text{vol}} = \sum_{e=1}^{n_{\text{el}}} M_e^{\text{vol}} \tag{9}$$

with the elementwise expansions, e.g. for the internal and the volume contributions

$$S_e^{\text{int}} = \sum_{n=1}^{n_{en}} \boldsymbol{w}_n \cdot \int_{\mathscr{B}_e} \boldsymbol{\sigma}^{\text{t}} \cdot \nabla_x N^n \, \mathrm{d}v \quad \text{and} \quad S_e^{\text{vol}} = \sum_{n=1}^{n_{en}} \boldsymbol{w}_n \cdot \int_{\mathscr{B}_e} \boldsymbol{b}^{\text{phy}} N^n \, \mathrm{d}v$$

$$M_e^{\text{int}} = \sum_{n=1}^{n_{en}} \boldsymbol{W}_n \cdot \int_{\mathscr{B}_{0e}} \boldsymbol{M}^{\text{t}} \cdot \nabla_X N^n \, \mathrm{d}V \quad \text{and} \quad M_e^{\text{vol}} = \sum_{n=1}^{n_{en}} \boldsymbol{W}_n \cdot \int_{\mathscr{B}_{0e}} \boldsymbol{B}^{\text{mat}} N^n \, \mathrm{d}V$$

Finally, considering the arbitrariness of the virtual physical and material node point displacements $\boldsymbol{w}_n$ and $\boldsymbol{W}_n$, we propose to compute global discrete physical and material node point forces as

$$\boldsymbol{F}^{\text{phy,nod}} = \mathop{\mathsf{A}}_{e=1}^{n_{\text{el}}} \int_{\mathscr{B}_e} \left[\boldsymbol{\sigma}^{\text{t}} \cdot \nabla_x N^n - \boldsymbol{b}^{\text{phy}} N^n \right] \mathrm{d}v \tag{10}$$

$$\boldsymbol{F}^{\text{mat,nod}} = \mathop{\mathsf{A}}_{e=1}^{n_{\text{el}}} \int_{\mathscr{B}_{0e}} \left[\boldsymbol{M}^{\text{t}} \cdot \nabla_X N^n - \boldsymbol{B}^{\text{mat}} N^n \right] \mathrm{d}V$$

In conclusion of the above considerations the discrete physical and material node point forces are thus energetically conjugated to variations of the physical and material node point positions. Moreover, the computation of the material node point forces involves the same operations as the computation of the physical node point forces which are already available for the solution of the direct motion problem and do therefore not contribute significantly to the overall computational costs.

Remark 4.1. It should be recalled that the discretized version of the quasi-static balance of physical momentum is used to solve the direct motion problem for given data contained in S^{sur} and S^{vol}. Then, the discretized version of the quasi-static balance of pseudo momentum is used in a post processing computation to evaluate the material node point forces from M^{int} and M^{vol} a posteriori.

Remark 4.2. It is interesting to note that the finite dimensional discrete physical and material node point forces preserve the properties of the corresponding balance equations of the underlying infinite-dimensional continuous setting which are discussed in detail in Part I of this work (Steinmann, 2001).

As an example the quasi-static equilibrium of physical and material forces is trivially satisfied elementwise due to the completeness condition $\sum_{n=1}^{n_{en}} N^n = 1$. As a consequence of the completeness condition constant fields render zero gradients with $\sum_{n=1}^{n_{en}} \nabla N^n = \nabla \sum_{n=1}^{n_{en}} N^n = \mathbf{0}$. For a verification it suffices to consider the internal contributions, e.g. to the discrete node point forces, of one element only

$$\sum_{n=1}^{n_{en}} \int_{\mathscr{B}_e} \boldsymbol{\sigma}^{\mathrm{t}} \cdot \nabla_x N^n \, \mathrm{d}v = \mathbf{0} \quad \text{and} \quad \sum_{n=1}^{n_{en}} \int_{\mathscr{B}_{0e}} \boldsymbol{M}^{\mathrm{t}} \cdot \nabla_X N^n \, \mathrm{d}V = \mathbf{0}$$

5. Comparison of alternative methods

In the sequel we compare alternative methods to compute the J-integral which was introduced to fracture mechanics by Rice (1968). Due to its definition as being energetically conjugated to crack extensions and its property of being path-independent the J-integral enjoys utmost popularity as a well-suited measure to assess fractured specimen.

To this end we consider an arbitrary subdomain $\mathscr{V}_0$ of the reference configuration $\mathscr{B}_0$. Thereby, the boundary $\partial\mathscr{V}_0$ is assumed to be decomposed into a regular and a singular part $\partial\mathscr{V}_0 = \partial\mathscr{V}_0^{\mathrm{r}} \cup \partial\mathscr{V}_0^{\mathrm{s}}$ with $\emptyset = \partial\mathscr{V}_0^{\mathrm{r}} \cap \partial\mathscr{V}_0^{\mathrm{s}}$. Then the singular part of $\partial\mathscr{V}_0$ denotes a crack tip with the unit vector $\boldsymbol{e}_{\parallel}$ pointing into the possible crack extension direction.

5.1. Contour integral method

The contour integral method was applied e.g. in the works of Shih and Needleman (1984a,b) among others. This method directly evaluates the line/surface integral as given by the J-integral along the regular part $\partial\mathscr{V}_0^{\mathrm{r}}$ of the contour $\partial\mathscr{V}_0 = \partial\mathscr{V}_0^{\mathrm{r}} \cup \partial\mathscr{V}_0^{\mathrm{s}}$ with $\emptyset = \partial\mathscr{V}_0^{\mathrm{r}} \cap \partial\mathscr{V}_0^{\mathrm{s}}$. Thereby, the J-integral reads e.g. in its scalar representation for the path independent case

$$J = \int_{\partial\mathscr{V}_0^{\mathrm{r}}} \boldsymbol{e}_{\parallel} \cdot \boldsymbol{M}^{\mathrm{t}} \cdot \boldsymbol{N} \, \mathrm{d}A \tag{11}$$

Here two different options are conceptually possible: either (a) the integration contour follows the element edges or (b) the integration contour directly connects the quadrature points of adjacent elements. Besides the computationally attractive theoretical independence of the results with respect to the integration contour this method has the drawbacks that it (i) requires additional FE data structure, (ii) leads to a possible loss of accuracy due to the numerical quadrature along the integration contour and (iii) involves additional overhead computations e.g. for the computation of the unit normal vector to the integration contour. The computational steps pertaining to the contour integral method are listed in Table 1.

Table 1
Computational steps for the contour integral method

(1) *Select integration contour*
(a) along element edges
(b) along quadrature points
(2) *Compute Eshelby stress at quadrature points*
(a) Project Eshelby stress to node points
(4) *Compute unit normal vector to integration contour*
(5) *Compute Eshelby traction at integration contour*
(6) *Integrate Eshelby traction along integration contour*

5.2. Domain integral method

The domain integral method was proposed in the works by Li et al. (1985) and Shih et al. (1986). Starting point for the domain integral method, which we shall review here for the materially homogeneous case only, is the definition of the scalar J-integral based on the singular part $\partial\mathscr{V}_0^{\mathrm{s}}$ of the contour $\partial\mathscr{V}_0 = \partial\mathscr{V}_0^{\mathrm{r}} \cup \partial\mathscr{V}_0^{\mathrm{s}}$ with $\emptyset = \partial\mathscr{V}_0^{\mathrm{r}} \cap \partial\mathscr{V}_0^{\mathrm{s}}$

$$J = -\int_{\partial\mathscr{V}_0^{\mathrm{s}}} \boldsymbol{e}_{\parallel} \cdot \boldsymbol{M}^{\mathrm{t}} \cdot \boldsymbol{N}\,\mathrm{d}A \tag{12}$$

With the introduction of a sufficiently smooth function, say $\bar{W} \in H^1(\mathscr{V}_0)$, which takes the value one on $\partial\mathscr{V}_0^{\mathrm{s}}$ and zero on $\partial\mathscr{V}_0^{\mathrm{s}}$ we obtain

$$J = -\int_{\partial\mathscr{V}_0^{\mathrm{r}} \cup \partial\mathscr{V}_0^{\mathrm{s}}} \bar{W}\boldsymbol{e}_{\parallel} \cdot \boldsymbol{M}^{\mathrm{t}} \cdot \boldsymbol{N}\,\mathrm{d}A = -\int_{\partial\mathscr{V}_0} \bar{\boldsymbol{W}} \cdot \boldsymbol{M}^{\mathrm{t}} \cdot \boldsymbol{N}\,\mathrm{d}A \quad \text{with } \bar{W} = \begin{cases} 1 & \text{on } \partial\mathscr{V}_0^{\mathrm{s}} \\ 0 & \text{on } \partial\mathscr{V}_0^{\mathrm{r}} \end{cases} \tag{13}$$

Next, due to the assumed smoothness of $\bar{W}$ we may apply the divergence theorem and partial integration and upon taking into account the assumed homogeneity, which manifests itself in $\mathrm{Div}\boldsymbol{M}^{\mathrm{t}} = \boldsymbol{0}$, we end up with

$$J = -\int_{\mathscr{V}_0} \left[\nabla_X \bar{\boldsymbol{W}} : \boldsymbol{M}^{\mathrm{t}} + \bar{\boldsymbol{W}} \cdot \mathrm{Div}\boldsymbol{M}^{\mathrm{t}}\right] \mathrm{d}V = -\int_{\mathscr{V}_0} \nabla_X \bar{\boldsymbol{W}} : \boldsymbol{M}^{\mathrm{t}}\,\mathrm{d}V \tag{14}$$

Finally, a standard Galerkin discretization of the preselected integration domain into $\bar{n}_{\mathrm{el}}$ elements with $\mathscr{V}_0^h = \cup_{e=1}^{\bar{n}_{\mathrm{el}}} \mathscr{B}_{0e}$ and the selection of prescribed virtual material displacements $\bar{\boldsymbol{W}}^h = \sum_{n=1}^{n_{en}} N^n \bar{\boldsymbol{W}}_n$ renders the algorithmic version of the domain integration method as proposed by Li et al. (1985)

$$J = -\sum_{e=1}^{\bar{n}_{\mathrm{el}}} \sum_{n=1}^{n_{en}} \bar{\boldsymbol{W}}_n \cdot \int_{\mathscr{B}_{0e}} \boldsymbol{M}^{\mathrm{t}} \cdot \nabla_X N^n\,\mathrm{d}V \tag{15}$$

Besides the usual sensitivity of the results with respect to the mesh design this method has the advantages that it (i) requires no additional FE data structure, (ii) is extremely versatile, (iii) is insensitive to the actual selection of the prescribed virtual material displacement and (iv) is insensitive to the actual selection of the integration domain. The computational steps pertaining to the domain integral method are listed in Table 2.

Table 2
Computational steps for the domain integral method

(1) *Select integration domain*
(2) *Prescribe virtual crack extension*
(3) *Compute Eshelby stress at quadrature points*
(4) *Perform standard numerical quadrature*

5.3. Material force method

Finally, the material force method advocated in this contribution might be summarized for the materially homogeneous case as follows

$$\boldsymbol{F}^{\mathrm{mat,nod}} = \mathop{\mathbf{A}}_{e=1}^{n_{\mathrm{el}}} \int_{\mathscr{B}_{0e}} \boldsymbol{M}^{\mathrm{t}} \cdot \nabla_X N^n\,\mathrm{d}V \tag{16}$$

Obviously, comparing Eqs. (15) and (16) it turns out that the material force method is intimately related to the domain integral method of Li et al. (1985). But, whereas the domain integral methods solely computes a

scalar energetic quantity associated with a configurational change, the material force method determines the vectorial force-like quantities conjugated to that configurational change. Clearly, vectorial quantities carry more information than scalar ones.

On the one hand, in the case of a singularity, e.g. for a crack, the length of the material force in the direction of the possible crack extension corresponds to the value of the J-integral. On the other hand we do not expect any discrete material forces in an otherwise homogeneous material. The presence of such spurious material forces indicates that a change of the node point positions of the discretization renders an improved mesh with less potential energy content, see also the reasoning by Braun (1997).

Finally, due to the interpretation of material forces as being energetically conjugate to configurational changes, discrete material forces at the boundary may be considered as a measure of the shape sensitivity of a specimen.

Thus, in anticipation of the results obtained in the next section, we may thus state that besides the usual sensitivity of the results with respect to the mesh design this method has the advantages that it (i) requires no additional FE data structure, (ii) is extremely versatile, (iii) renders additional indicators for the geometrical shape sensitivity of the specimen and (iv) renders additional indicators for the mesh quality. The computational steps pertaining to the material force method are listed in Table 3.

Table 3
Computational steps for the material force method

(1) *Compute Eshelby stress at quadrature points*
(2) *Perform standard numerical quadrature*

Thus the method simply consists in the determination of the material node point forces corresponding to the Eshelby stress which are trivially computable after the direct motion problem has been solved. It will be demonstrated in the sequel that these material node point forces may effectively be used for the assessment of fractured configurations of hyperelastic material.

6. Examples

In this section we focus on the computational performance and versatility of the proposed material force method. To this end we first reinvestigate the classical interface problem in a hyperelastic bi-material bar in one dimension in order to emphasize the relevant concepts of our approach. In the sequel, we study the results obtained with the material force method with those obtained from the classical J-integral evaluation for some standard fracture mechanics specimen in the geometrically linear setting. Moreover we focus on the influence and the delicate implications of the mesh design on the results obtained. Next we compare the results from the geometrically linear treatment with those of a fully geometrically nonlinear computation for the example of a single edge notched specimen in tension (SET). Here we emphasize the intuitively obvious result that the consideration of geometrically nonlinear effects leads to reduced loading by material forces due to the blunting of the crack tip. Finally, as an outlook to further investigations, we highlight the applicability of the proposed method to other types of singularities as present in wedged specimen and to defect configurations like soft and rigid inclusions.

6.1. Hyperelastic bi-material 1D bar in tension

This example is intended to illustrate on the one hand the aforementioned material quantities and to illuminate on the other hand the proposed finite element approach to compute discrete material node point forces. The elementary linear theory of beams has been analyzed within the framework of material forces

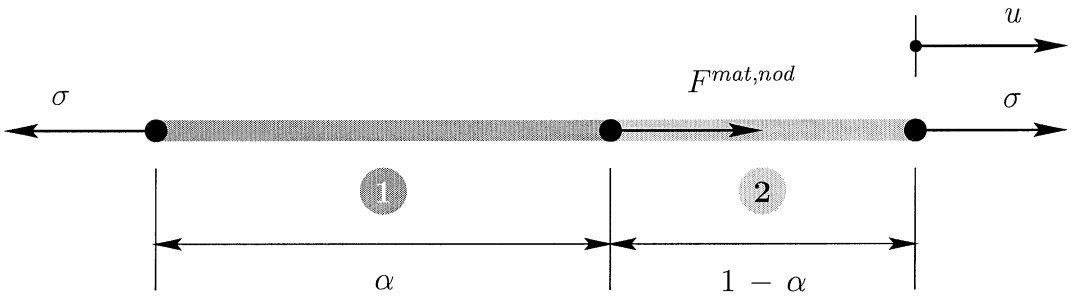

Fig. 1. Hyperelastic bi-material 1D bar in tension.

extensively by Kienzler and Herrmann (1986a,b) and Kienzler (1986). Here we shall consider the even simpler problem of a bi-material hyperelastic bar under tension in Fig. 1, nevertheless for the more general geometrically nonlinear case. The bar has unit length and is discretized by two 1D finite elements. One part of the bar with length α consists of an arbitrary hyperelastic material 1 while the remaining part of the bar with length $1-\alpha$ consists of an arbitrary hyperelastic material 2. Due to physical equilibrium the Cauchy stress σ in the bar is constant, moreover the stretches in both parts of the bar are constant and can be evaluated conceptually by the inversion of the hyperelastic constitutive laws

$$\sigma_1 = \partial_\lambda \mathscr{W}_{01} = \partial_\lambda \mathscr{W}_{02} = \sigma_2 \quad \Rightarrow \quad \lambda_1 = [\sigma_1(\lambda_1)]^{-1} \quad \text{and} \quad \lambda_2 = [\sigma_2(\lambda_2)]^{-1}$$

Then constant Eshelby stresses in the two parts of the bar follow as

$$M_1 = \mathscr{W}_{01} - \lambda_1\sigma \quad \text{and} \quad M_2 = \mathscr{W}_{02} - \lambda_2\sigma$$

Within a finite element discretization constant Eshelby stresses in 1D render the material node point forces at the element level as

$$\left[\int_{\mathscr{B}_{0e}} MN^n_{,X}\,\mathrm{d}X\right] = M[N^n]_{\xi=-1}^{\xi=1} = M[-1,0,\ldots,0,1]$$

Here we exploited the property of the shape functions $N^n(\xi_m) = \delta_{nm}$ whereby $\xi = \pm 1$ denote the isoparametric coordinates at the beginning and the end of a 1D element.

Based on these intermediate results the material node point force at the interface of the two materials is computed after the assembly of the discretized element contributions with $[\![\bullet]\!]$ denoting the jump $[\bullet]_1 - [\bullet]_2$ as

$$F^{\mathrm{mat,nod}} = [\![\mathscr{W}_0]\!] - [\![\lambda]\!]\sigma$$

For an interpretation of this quantity we first compute the material sensitivity of the stretches from the total elongation between the ends of the bar, i.e. the sensitivity at fixed deformed configuration which is consistent with our theoretical set up in Part I of this work (Steinmann, 2001)

$$u = \lambda_1\alpha + \lambda_2[1-\alpha] - 1 \quad \Rightarrow \quad \delta_\alpha u = \delta_\alpha\lambda_1\alpha + \delta_\alpha\lambda_2[1-\alpha] + [\![\lambda]\!]\delta\alpha = 0$$

Then the material variation, i.e. the variation at fixed deformed configuration, of the total stored energy follows as

$$W = \int_{\mathscr{B}_{0e}} \mathscr{W}_0\,\mathrm{d}X = \mathscr{W}_{01}\alpha + \mathscr{W}_{02}[1-\alpha] \quad \Rightarrow \quad \delta_\alpha W = \delta\alpha[[\![\mathscr{W}_0]\!] - [\![\lambda]\!]\sigma]$$

Remarkably, we obtain formaly exactly the same result for $\delta_\alpha W$ if we allow for a less abstract $\delta_\alpha u \neq 0$, i.e. if we allow the deformed configuration to change due to the change of the undeformed configuration, and thus consider additionally the change of the external potential energy. In conclusion, in view of the

definition of the material node point force at the interface, $F^{\mathrm{mat,nod}}$ is interpreted as energetically conjugated to a variation $\delta\alpha$ of the position of the bi-material interface. A similar expression for the material force acting on an interface has been derived via different arguments e.g. by Hill (1986).

6.2. Geometrically linear specimen with crack

Next, we consider SET, double edge notched (DET) and center cracked (CCT) fracture mechanics specimen in tension with plane strain constraint. The height to width ratio is $H/W = 3/1$, the ratio of the crack length to the width is $a/W = 1/2$, the specimen has unit width. The specimen are discretized by bi-quadratic $S2$-serendipity elements, the mesh is heavily densified around the crack tip. Moreover the elements at the crack tip are degenerated into triangles with the midside nodes on those edges emanating radially from the crack tip shifted to the quarter point positions. It is known that by this modification of the original element set-up the $r^{-(1/2)}$ singularity in the strains and stresses typical for geometrically linear elasticity is nicely captured. The material is modelled by isotropic linear Hooke elasticity with Young's modulus $E = 206.9 \times 10^3$ N/mm^2 and Poisson's ratio $\nu = 0.29$ corresponding roughly to a steel. A constant distributed tensile load of 10 N/mm^2 is applied at the top surface, the lateral movement of the nodes at the top and bottom surface are unconstrained.

The computed discrete material node point forces are depicted in Fig. 2 together with a zoom of the typical scenario at the crack tip. Thereby material forces point into the direction of a potential energy

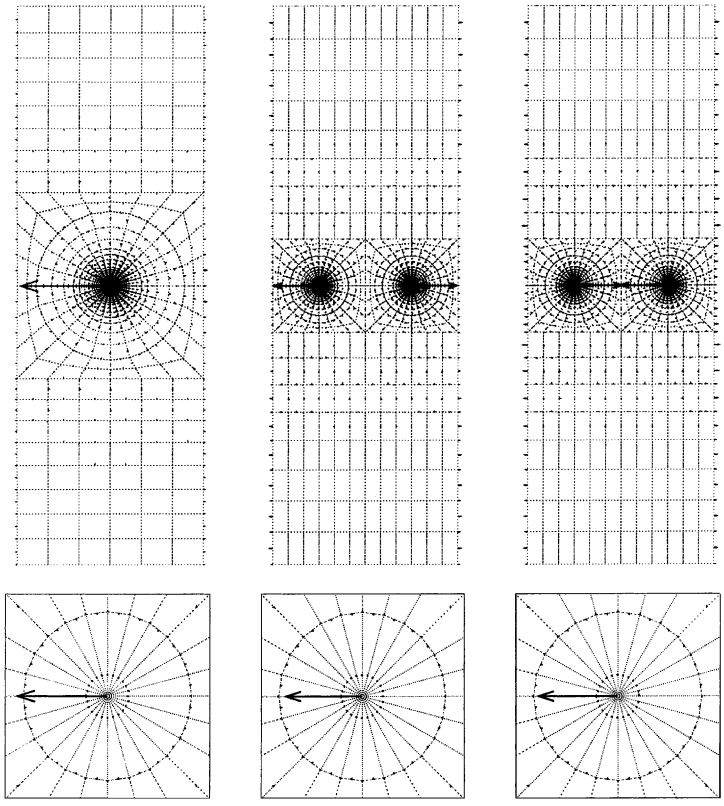

Fig. 2. Discrete material node point forces for the geometrically linear SET, DET & CCT specimen. Material forces point into the direction of potential energy increase upon replacement of the material node point position.

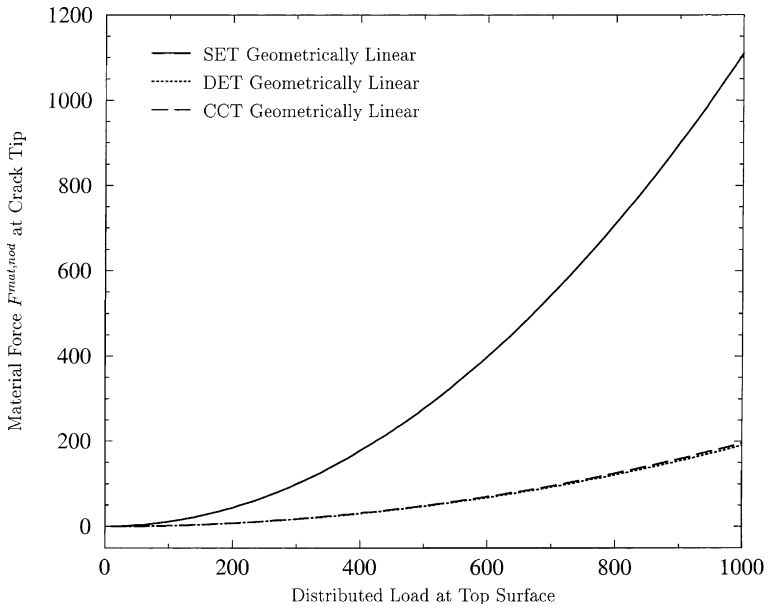

Fig. 3. Discrete material node point force at the crack tip over the amount of loading. The quadratic dependence is typical for linear elasticity with a stored energy quadratic in the displacement gradients.

increase upon replacement of the material node point position. Thus the growth of the crack in the direction opposite to the material force, i.e. the replacement of the material position of the crack tip node point that enlarges the crack length, corresponds to a decrease of the potential energy. Please note that we observe additional small material forces at the boundaries of the specimen indicating that the potential energy content of the specimen will also change if the initial geometry of the specimen is changed. This is obviously an additional information that is not provided by any other computational method described above. Next, Fig. 3 displays the quadratic dependence of the discrete material node point force at the crack tip on the amount of loading as typical for linear elastic problems.

Moreover Table 4 summarizes the comparison of the discrete material node point forces with reference values for the classical J-integral which are taken from Rooke and Cartwright (1976). It is remarkable that the results obtained with the material force method as proposed in this contribution differ only slightly from the reference results, i.e. the maximum deviation is less than 2%.

Next, we investigate the sensitivity of the results with respect to the mesh design. It may be shown that an optimal result in the sense of representing the correct singularity in the strains and stresses is obtained if the $S2$-elements at the crack tip are degenerated into triangles with the midside nodes on those edges emanating radially from the crack tip shifted to the quarter point positions with $r/L = 0.25$. In this case the typical $r^{-(1/2)}$ singularity in the strains and stresses is exactly captured. Therefore we study the influence of shifting

Table 4
Comparison of discrete material node point forces with analytical values for the J-integral

Specimen type	$\frac{J_1}{(\sigma^2 \pi a/E')}$ table	$\frac{F_1^{\mathrm{mat,nod}}}{(\sigma^2 \pi a/E')}$ code	Deviation (%)
SET	8.079	7.978	1.253
DET	1.392	1.367	1.777
CCT	1.382	1.408	1.868

The maximum deviation is less than 2%.

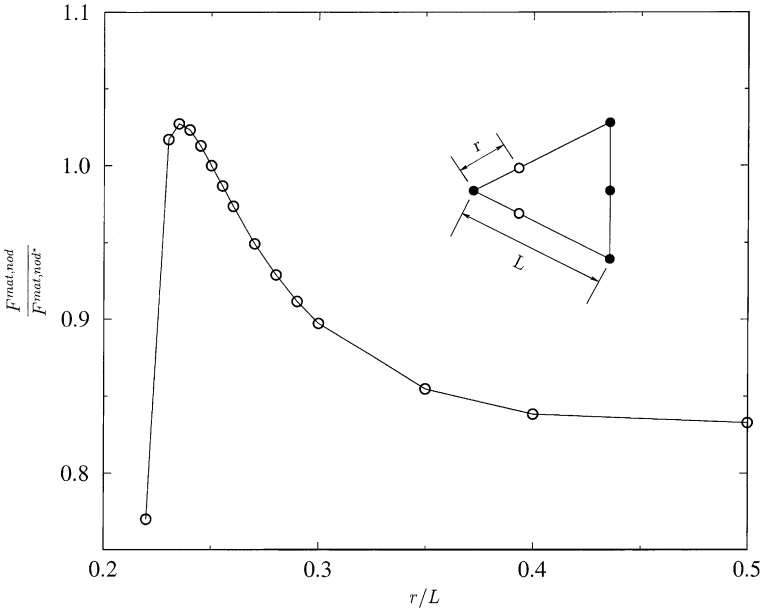

Fig. 4. Variation of normalized discrete material node point forces with placement of element edge node point of innermost ring of elements. The sensitivity of the results is less than 17%.

the edge nodes of the innermost ring of elements to positions different from this optimal case. The resulting normalized discrete material node point forces for the SET specimen are displayed against the midside node point position in Fig. 4. It can be observed that the exact value is obtained for $r/L = 0.25$. Already slight deviations from this position render pertubations of the correct result. Nevertheless it appears that for reasonable placement of the midside node in the range $r/L \in [0.25, 0.50]$ the deviation is less than 17%.

Finally, the resulting spatial distribution of discrete material node point forces in the vincinity of the crack tip are displayed in Fig. 5 for the cases $r/L = 0.245, 0.250, 0.255, 0.500$. Remarkably, nonoptimal discretizations are indicated by small spurious material forces at internal node points which show up besides the dominant material force at the crack tip. These spurious material forces exceed the tolerance used for the residuum of the direct motion problem and are not to be confused with the noise due to round-off errors which always renders nodal values in the order of the machine precision. Thus the material force method renders additional informations about the quality of the discretization. Interesting enough, related observations constitute the underlying motivation for the node point relocation method as advocated by Braun (1997) which aims in an optimal node point distribution at fixed mesh topology such that spurious material forces are minimized. Thus, as a rule, the optimal discretization is characterized by a minimum of spurious material forces. Nevertheless, summing up the spurious material forces renders a value that slightly improves upon the material force at the crack tip with regard to the value of the J-integral.

6.3. Geometrically nonlinear specimen with crack

In the following example we study the influence of a geometrically nonlinear treatment. To this end we consider a plane strain SET specimen in tension with geometry and discretization as in the previous example. The material is modelled by isotropic nonlinear quasi-incompressible Neo-Hooke elasticity based on the stored energy function $\mathscr{W}_0 = 0.5\mu[I_1 - 3] - \mu \ln J + 0.5\lambda[\ln J]^2$ with Young's modulus $E = \mu[3\lambda + 2\mu]/[\lambda + \mu] = 50 \times 10^3$ N/mm^2 and Poisson's ratio $\nu = 0.5\lambda/[\lambda + \mu] = 0.45$ corresponding roughly to a

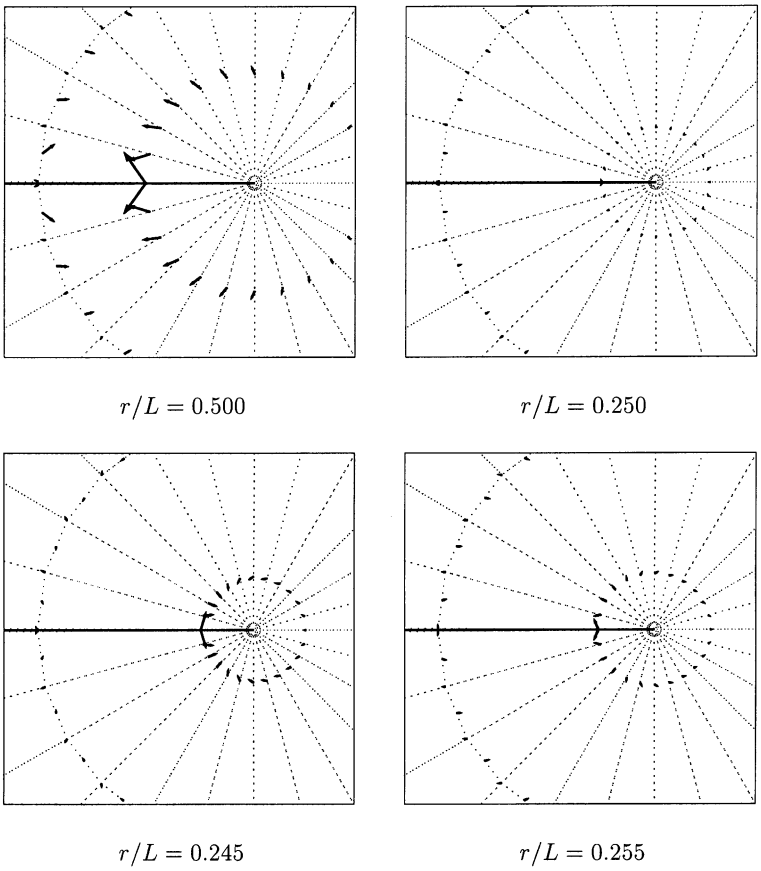

Fig. 5. Zoom of the crack tip vicinity showing additional spurious discrete material node point forces if the discretization does not caputure exactly the correct singularity.

rubber. A constant elongation of $16.\bar{6}\%$ is applied incrementally by prescribed displacements at the top surface, the lateral movement of the nodes at the top and bottom surface are unconstrained.

The computed discrete material node point forces at the end of the load history are depicted in Fig. 6(b) together with a zoom of the typical scenario at the crack tip. Obviously, besides the single material force at the crack tip, a number of spurious material forces are present that indicate indirectly that the type of singularity of the solution has changed with respect to the geometrically linear solution. In fact, due to the blunting of the crack tip, the resulting stress intensity appears to be less critical.

This is clearly demonstrated by elongating the specimen without taking into account the geometrical nonlinearities. Thus the typical $r^{-(1/2)}$ singularity is present in the strains and stresses. Since it is exactly captured by the discretization invoked, no spurious material forces are visible in Fig. 6(a). Please note that the material forces in Fig. 6(a) and (b) are scaled similarly.

Along the same lines, Fig. 7 displays the dependence of the discrete material node point force at the crack tip on the amount of loading in comparison with the geometrically linear case. Thereby, the material force is normalized with respect to the material force of the geometrically linear solution. In the initial loading phase geometrical stiffening effects seem to prevail but with increased loading a clear drop of the normalized material force is observable, thus indicating again a less critical stress intensity in comparison with the geometrically linear solution.

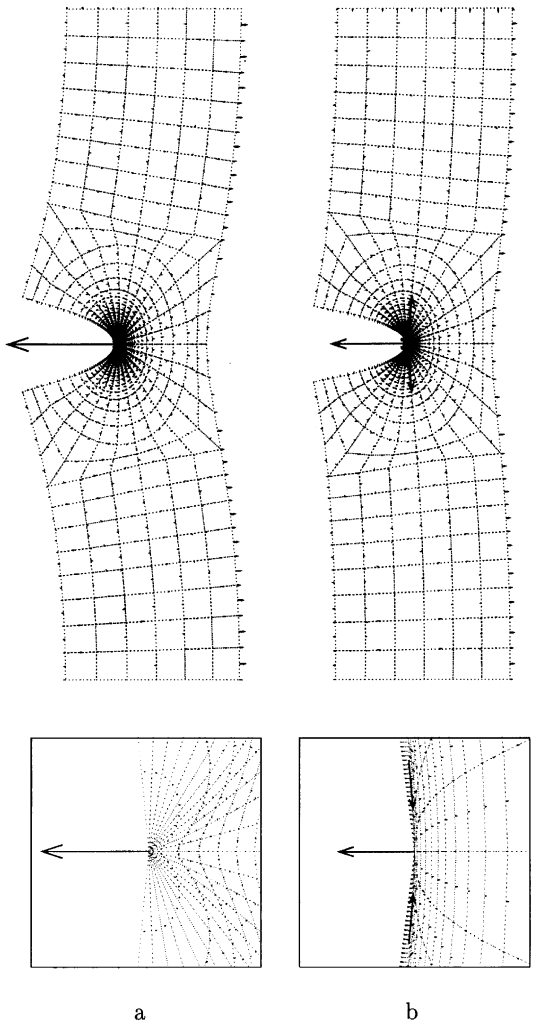

Fig. 6. (a) Discrete material node point forces for the geometrically linear SET specimen at 16.$\bar{6}$% elongation. No spurious material forces are present since the type of singularity is exactly captured. (b) Discrete material node point forces for the geometrically nonlinear SET specimen at 16.$\bar{6}$% elongation. Spurious material forces indicate indirectly that the type of singularity has changed w.r.t. the geometrically linear case.

6.4. Geometrically linear specimen with wedge

Next, we investigate how the discrete material node point forces are quantitatively influenced by varying the singularity in the strains and stresses for the geometrically linear case. To this end we consider specimen in tension with a wedge and plane strain constraint, whereby we vary the opening angle of the wedge in the range 0°, 30°, 60°, 90°. For a wedged configuration the singularity in strains and stresses varies between $r^{-0.500}$ at an opening angle of $\beta = 0°$, i.e. for a crack, and $\approx r^{-0.455}$ at an opening angle of $\beta = 90°$. These results are taken from suited solutions of the analytical eigenvalue equation $\sin(2\pi\lambda - [\lambda + 1]\beta) - [\lambda + 1]\sin\beta = 0$ in terms of the exponent r^{λ} and the opening angle β. The geometry and the discretization are the same as in the previous examples, whereby only the wedge is cut out of the mesh. The material is modelled again by

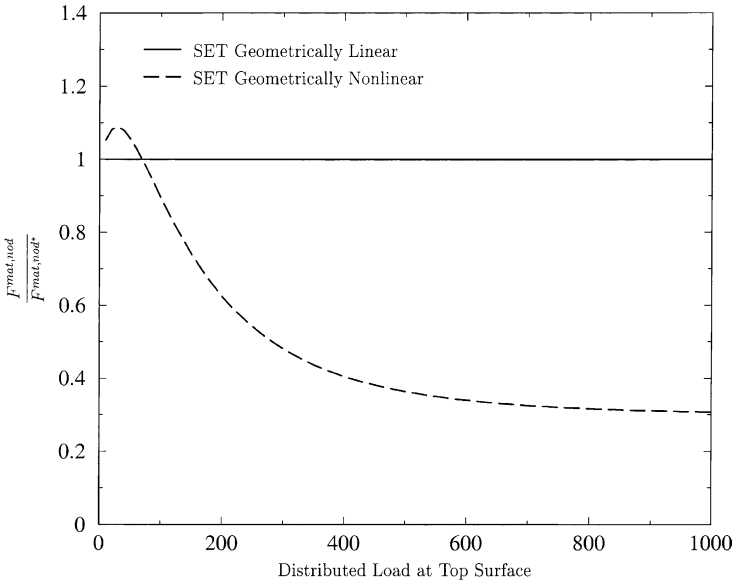

Fig. 7. Discrete material node point force at the crack tip over the amount of loading.

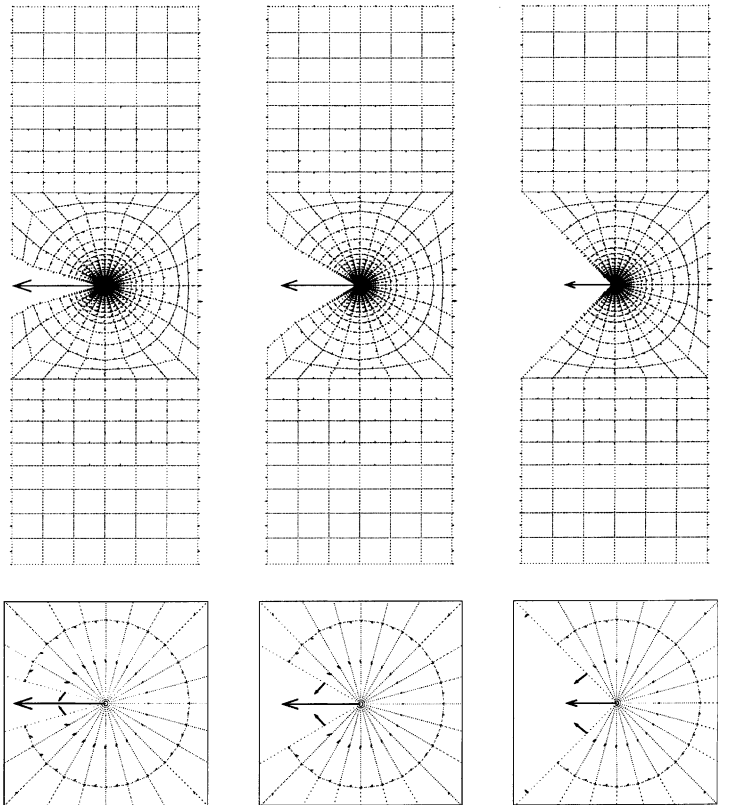

Fig. 8. Discrete material node point forces for the geometrically linear specimen with wedge $[30°, 60°, 90°]$. It appears that material forces scale with the opening angle.

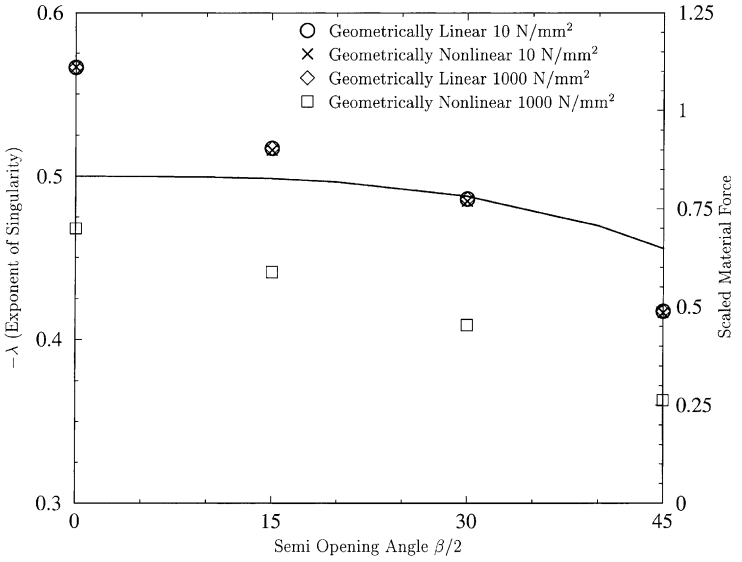

Fig. 9. Discrete material node point forces for the geometrically linear specimen with wedge contrasted to the type of singularity. It appears that material forces scale nonlinearily with the type of singulartity.

isotropic linear Hooke elasticity with Young's modulus $E = 206.9 \times 10^3$ N/mm^2 and Poisson's ratio $\nu = 0.29$ corresponding roughly to a steel. A constant distributed tensile load of 10 N/mm^2 is applied at the top surface, the lateral movement of the nodes at the top and bottom surface are unconstrained.

The computed discrete material node point forces are depicted in Fig. 8 together with a zoom of the typical scenario at the wedge tip. The quantitative change of the material forces with the type of singularity is clearly visible, see also Fig. 9. From these results it appears that the discrete material node point forces are a similar measure as the stress intensity at the wedge tip. Similar to the previous examples, we observe again spurious small material forces inside the domain in the vicinity of the wedge tip. Thus, as a interpretation, a non optimal mesh design is indicated by the material force method. Nevertheless, strategies of how to adapt meshes in order to minimize spurious material forces are not in the scope of the present investigation.

6.5. Geometrically linear specimen with inclusion

Finally, we consider specimen with a circular inclusion in tension with plane strain constraint. Thereby, no singularities are present in the solution, thus the precise mesh design is less delicate. The geometry and the discretization are the same as in the previous examples, whereby the ratio of the inclusion radius to the specimen width is $R/W = 0.1$. The bulk material is modelled by isotropic linear Hooke elasticity with Young's modulus $E = 206.9 \times 10^3$ N/mm^2 and Poisson's ratio $\nu = 0.29$ corresponding roughly to a steel. For the soft inclusion, the Young's modulus is approximately set to $E \approx 0$, the rigid inclusion is modelled by setting the Young's modulus approximately to $E \approx \infty$. A constant distributed tensile load of 10 N/mm^2 is applied at the top surface, the lateral movement of the nodes at the top and bottom surface are unconstrained.

The computed discrete material node point forces for the soft and the rigid inclusions are depicted in Fig. 10 together with zooms of the typical scenario at the inclusion. Here, discrete material node point forces mark the interface between the inclusion and the bulk material. Recall that material forces point into the direction of a potential energy increase upon replacement of the material node point position. Thus for the

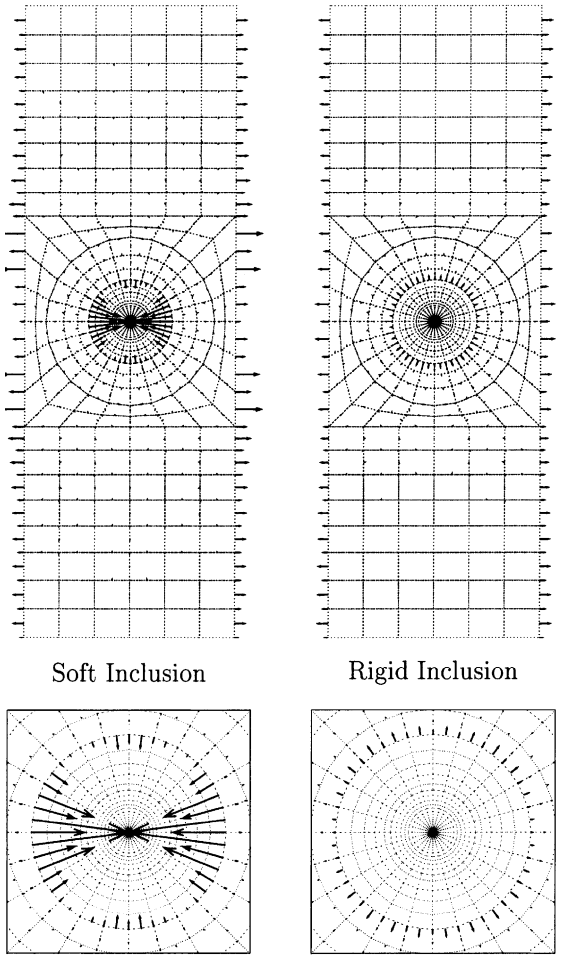

Fig. 10. Discrete material node point forces for the geometrically linear specimen with inclusion. Material forces point into the direction of potential energy increase upon replacement of the material node point position.

soft inclusion the growth of the inclusion into an ellipsoid and for the rigid inclusion the shrinkage of the inclusion into an ellipsoid, i.e. a morphology change in the direction opposite to the material force, corresponds to a decrease of the potential energy content of the specimen. The equilibrium shape of inclusions has been considered numerically by an alternative strategy by Schmidt and Gross (1995, 1997). Obviously, the discrete material node point forces computed by the present proposal may be considered as the driving forces for the kinetics of morphology changes.

7. Conclusions

The objective of this work was to exploit the concept of material forces as advocated by Maugin (1993) to develop a novel algorithmic treatment of problems within hyperelastostatic fracture mechanics. To this

end, the so-called balance of pseudo momentum in the material manifold is recast in weak form, cf. to Part I of this work (Steinmann, 2001). This variational statement then lends itself in a straightforward manner to a standard Galerkin type finite element discretization. Thereby, the discrete material node point forces take the interpretation as being energetically conjugated to variations of the material node point positions. It is remarkable from the implementational point of view that the computation of the discrete material node point forces involves only operations which are already available for the solution of the direct motion problem. Thus the conceptual beauty of material forces is accompanied by an extremely simple implementation which makes the advocated approach favorable in comparison with alternative methods.

The examples clearly demonstrated that for fracture mechanics problems the discrete material node point forces at the crack tip coincide with the celebrated J-integral. Nevertheless, the examples emphasized moreover that material forces render a number of additional informations, namely (i) on the energetic sensitivity of the specimen geometry and (ii) on the discretization quality. These aspects are up to now not fully exploited and will therefore constitute an area of further research. Moreover, the present approach is applicable to general problems of defect mechanics. This additional potential was highlighted for the case of specimen with interfaces, wedges or inclusions. Again the systematic investigation of these aspects is in the focus of our future research. Finally the extension to inelastic material response, coupled fields and in general the kinetics of defects is certainly within the realm of the conceptual potential of material forces.

References

Anderson, T.L.,1995. Fracture Mechanics: Fundamentals and Applications. CRC Press, Boca Raton.

Braun, M., 1997. Configurational forces induced by finite-element discretization. Proc. Estonian Acad. Sci. Phys. Math. 46, 24–31.

Delorenzi, H.G., 1982. On the energy release rate and the J-integral for 3-D crack configurations. Int. J. Fract. 19, 183–193.

Delorenzi, H.G., 1985. Energy release rate calculations by the finite element method. Engr. Fract. Mech. 21, 129–143.

Hellen, T.K., 1975. On the method of virtual crack extensions. Int. J. Num. Meth. Engr. 9, 187–207.

Hill, R., 1986. Energy-momentum tensors in elastostatics: some reflections on the general theory. J. Mech. Phys. Solids 34, 305–317.

Kienzler, R., 1986. On existence and completeness of conservation laws associated with elementary beam theory. Int. J. Solids Struct. 22, 789–796.

Kienzler, R., Herrmann, G., 1986a. An elementary theory of defective beams. Acta Mechanica 62, 37–46.

Kienzler, R., Herrmann, G., 1986b. On material forces in elementary beam theory. J. Appl. Mech. 53, 561–564.

Li, F.Z., Shih, C.F., Needleman, A., 1985. A comparison of methods for calculating energy release rates. Engr. Fract. Mech. 21, 405–421.

Maugin, G.A., 1993. Material Inhomogeneities in Elasticity. Chapman and Hall, London.

Moran, B., Shih, C.F., 1987. A general treatment of crack tip contour integrals. Int. J. Fract. 35, 295–310.

Parks, D.M., 1974. A stiffness derivative finite element technique for determination of crack tip stress intensity factors. Int. J. Fract. 10, 487–502.

Parks, D.M., 1977. The virtual crack extension method for nonlinear material behaviour. Comp. Meth. Appl. Mech. Engr. 12, 353–364.

Rice, J.R., 1968. A path independent integral and the approximate analysis of strain concentration by notches and cracks. J. Appl. Mech. 35, 379–386.

Rooke, D.P., Cartwright, D.J., 1976. Compendium of stress intensity factors HMSO. Hillingdon Press, Uxbridge.

Schmidt, I., Gross, D., 1995. A strategy for determining the equilibrium shape of an inclusion. Arch. Mech. 47, 379–390.

Schmidt, I., Gross, D., 1997. The equilibrium shape of an elastically inhomogeneous inclusion. J. Mech. Phys. Solids 45, 1521–1549.

Shih, C.F., Needleman, A., 1984a. Fully plastic crack problems. Solutions by a penalty method. Part I ASME J. Appl. Mech. 51, 48–56.

Shih, C.F., Needleman, A., 1984b. Fully plastic crack problems. Application of consistency checks. Part II ASME J. Appl. Mech. 51, 57–64.

Shih, C.F., Moran, B., Nakamura, T., 1986. Energy release rate along a three-dimensional crack front in a thermally stressed body. Int. J. Fract. 30, 79–102.

Steinmann, P., 2001. Application of material forces to hyperelastostatic fracture mechanics. Part I: Continuum mechanical setting. Int. J. Solids Struct. 37, 7371–7391.